A new method to assess mesoscale contributions to meridional heat transport in the North Atlantic Ocean

Andrew Delman[1] and Tong Lee[1]

[1]Jet Propulsion Laboratory, California Institute of Technology, Pasadena, CA, USA

Correspondence: Andrew Delman (adelman@jpl.caltech.edu)

Abstract. The meridional heat transport (MHT) in the North Atlantic is critically important to climate variability and the global overturning circulation. A wide range of ocean processes contribute to North Atlantic MHT, ranging from basin-scale overturning and gyre motions to mesoscale instabilities (such as eddies). However, previous analyses of "eddy" MHT in the region have mostly focused on the contributions of time-variable velocity and temperature, rather than considering the spatial scales that are more fundamental to the physics of ocean eddies. In this study, a zonal spatial-scale decomposition separates large-scale from mesoscale velocity and temperature contributions to MHT, in order to characterize the physical processes driving MHT. Using this approach, we found that the mesoscale contributions to the time mean and interannual/decadal (ID) variability of MHT in the North Atlantic Ocean are larger than large-scale horizontal contributions, though smaller than the overturning contributions. Considering the 40° N transect as a case study, large-scale ID variability is mostly generated in the deeper part of the thermocline, while mesoscale ID variability has shallower origins. At this latitude, most ID MHT variability associated with mesoscales originates in two regions: a western boundary region (70°–60° W) associated with 1–4 year interannual variations, and an interior region (50°–35° W) associated with decadal variations. Surface eddy kinetic energy is not a reliable indicator of high MHT episodes, but the large-scale meridional temperature gradient is an important factor, by influencing the local temperature variance as well as the local correlation of velocity and temperature. Most of the mesoscale contribution to MHT at 40° N is associated with transient and propagating processes, but stationary mesoscale dynamics contribute substantially to MHT south of the Gulf Stream separation, highlighting the differences between the temporal and spatial decomposition of meridional temperature fluxes.

1 Introduction

Meridional heat transport (MHT) is essential to both the mean and variability of global climate. The time-mean MHT in the ocean is substantially lower than that in the atmosphere in mid-latitudes Trenberth and Caron (2001). However, oceanic MHT variability is important to the time variability of heat transport in the Earth system, particularly on interannual and de-

cadal timescales (e.g., Häkkinen, 1999). Oceanic MHT is primarily associated with several physical processes: (1) overturning
25 circulations with zonal-mean flows in distinct depth ranges carrying waters of different temperatures, (2) gyre circulations
advecting waters of different temperatures at distinct longitudes, and (3) mesoscale dynamics including coherent vortices ("ed-
dies") developing from flow instabilities, as well as mesoscale-intensified jets and recirculations that are sustained by nonlinear
momentum advection and rectified eddy fluxes (e.g., Hoskins et al., 1983; Waterman and Hoskins, 2013; Delman et al., 2015).
Due to the steep vertical temperature gradients in much of the ocean, the overturning contribution to MHT has received the
30 most attention in observational analyses of MHT (e.g., Talley, 2003, for a discussion of overturning MHT contributions)

The Atlantic basin has attracted particular interest in studies of the oceanic MHT, because of the role of the Atlantic Me-
ridional Overturning Circulation and its implications for regional and global climate. The MHT in the north Atlantic ocean
has been estimated as the transport required to balance air-sea heat flux observations (Hsiung, 1985) and as the residual from
the top-of-atmosphere radiation balance that is unexplained by atmospheric transport (Trenberth and Caron, 2001); however,
35 these methods of quantifying MHT are only useful for time-mean MHT since the time-mean change in heat storage is small
compared to radiative fluxes and heat transports. Estimates of MHT have also been derived from in-situ measurements by
ships (e.g., Hall and Bryden, 1982, and references therein; Koltermann et al., 1999; Talley, 2003) and autonomous Argo flo-
ats (Hobbs and Willis, 2012). Moreover, oceanic MHT at 24–26.5°N has been estimated using observations from the Rapid
Climate Change-Meridional Overturning Circulation and Heatflux Array (RAPID-MOCHA) of moorings (Johns et al., 2011).
40 Yet explicit estimates of MHT from ocean observations are often based on sparsely distributed measurements, and are likely
to underestimate the contribution of mesoscale dynamics. Johns et al. (2011) estimated an Atlantic "eddy" MHT contribution
of 0.10±0.03 PW at 24°-26°N based on spatially covarying velocity and temperature in five hydrographic sections, which is
small compared to the estimated ~1.3 PW total MHT at these latitudes. However, ship-based measurements do not generally
show the full scope of MHT variability at a given latitude, and in the Atlantic there is far more mesoscale activity where the
45 Gulf Stream separates from the western boundary.

Ocean models, particularly high-resolution eddy-permitting general circulation models (GCM), have been valuable tools
to estimate the time mean MHT as well as its variability. An important caveat is that most of these studies consider any
deviation of velocity or temperature from time-mean values to be an "eddy" contribution to MHT. Using a 1/4° resolution
ocean GCM, Jayne and Marotzke (2002) estimated the time mean northward eddy MHT in the North Atlantic to peak at
50 approximately 0.1 PW near 40°N, a smaller contribution than they found in tropical basins. Despite this relatively small value,
and the fact that the grid resolution 1/4° is insufficient to resolve the baroclinic deformation radius at 40°N (Hallberg, 2013),
time-mean maps of temperature fluxes in the Jayne and Marotzke study display many mesoscale features. Using a higher-
resolution 1/12° model, Tréguier et al. (2017) found somewhat higher time-mean values of the eddy heat flux near 40°N,
with a sharper peak of approximately 0.3 PW at 36.6°N near the Gulf Stream separation. Volkov et al. (2008) used a state
55 estimate with mean horizontal grid spacing of 18 km, and limited the definition of eddy heat flux to comprising velocity and
temperature anomalies at timescales shorter than 3 months; they found much smaller time-mean eddy heat fluxes (near zero
at 40°N), though with a temporal standard deviation slightly over 0.1 PW. The results of these studies imply that eddy heat
fluxes are dependent not just on model resolution, but on how "eddies" are defined. A canonical eddy is typically a vortex that

is no more than a few hundred kilometers in diameter (i.e., mesoscale), but model analyses have not yet (to our knowledge)
60 quantified basin-integrated temperature fluxes according to the spatial scale of the processes driving the fluxes. Moreover,
observational estimates that use (remote sensing-based) eddy tracking methods to quantify eddy contributions to heat transport
(e.g., Hausmann and Czaja, 2012; Dong et al., 2014; Sun et al., 2019) have reached divergent conclusions depending on the
methodology and scope of what is considered part of the eddy transport. One way to address this ambiguity is to consider
the impact of all mesoscale dynamics on meridional heat transport, whether or not these mesoscale fluxes are due to coherent
65 vortices.

The focus of this study is to quantify the time-mean and time-variable contribution of mesoscale dynamics to meridional
heat transport in the North Atlantic, with a particular focus at 40°N where the Gulf Stream extension is nearly zonal and eddy
kinetic energy (EKE) is near its maximum. Section 2 will discuss the eddy-permitting model simulation and the framework
used to decompose the temperature fluxes into overturning, large-scale, and mesoscale components. Section 3 summarizes
70 the results and the cross-basin structure of mesoscale temperature fluxes, while Section 4 relates the variability of mesoscale
temperature fluxes to other indicators of the ocean state such as EKE and meridional temperature gradient. Section 5 discusses
novel aspects of the approach presented here and compared to earlier formulations of eddy fluxes, while Section 6 summarizes
the conclusions of this study.

2   Methods

2.1   Model simulation and data

Most of our analysis uses output from a numerical simulation of the Parallel Ocean Program (POP) 2, a primitive equation
ocean model (Smith et al., 2010). POP is the ocean component of the Community Earth System Model framework, and in this
simulation it was configured on a tripole grid with two north poles over Canada and Siberia—more details of the simulation
are found in Johnson et al. (2016) and Delman et al. (2018). The simulation was run on the Yellowstone computing cluster
80 (Computational and Information Systems Laboratory, 2016) with a resolution of 0.1° at the equator, and approximately 8
km in the mid-Atlantic; it was forced with Coordinated Ocean-Ice Reference Experiments version 2 (CORE.v2; Large and
Yeager, 2009), an interannually-varying flux dataset based on the National Centers for Environmental Prediction reanalysis
with corrections from various satellite data. State variables (including velocity and temperature) and temperature fluxes have
been archived from this simulation in 5-day averages, facilitating studies of mesoscale processes which frequently vary on
85 intraseasonal timescales.

In addition to the model simulation output, the ocean surface dynamic topography dataset merged from various altimeters
is used to validate the model's mean state and its representation of ocean surface variability. This dataset is produced by
Collecte Localisation Satellites (Ducet et al., 2000) and available through the Copernicus Marine Environment Monitoring
Service (CMEMS) at 1/4° spatial and daily temporal resolution. Compared to the altimetry-based dynamic topography, the
90 model reproduces most essential features of the circulation in the North Atlantic (Fig. 1), though there are several important
issues that have been previously noted in other model simulations (for a review of these issues see Chassignet and Marshall,

2008). These include the Gulf Stream separating from the continental slope at 38°-39°N in the model (Fig. 1b) vs. ~36°N in observations (Fig. 1a), and too low eddy kinetic energy in the Northwest Corner region near 50°N, 40°W and in the Azores Current region near 34°N (Fig. 1c,d). These inaccuracies have been resolved in regional simulations of the North Atlantic at 95   1/10° resolution (e.g., Bryan and Smith, 1998; Smith et al., 2000; Bryan et al., 2007), but persist in global simulations even at the same resolution (e.g., Maltrud and McClean, 2005; Kirtman et al., 2012; Griffies et al., 2015). Therefore the focus of this study is on 40°N, in between the Gulf Stream Separation and the Northwest Corner where the distribution of EKE in the model is qualitatively similar to observations (Fig. 1c,d). The zonally-averaged values of EKE at 40°N are lower in POP than in the altimetry data, but this is true of much of the North Atlantic, and the zonally-averaged EKE peaks in altimetry and in the 100   model are both at latitudes near 40°N (Fig. 1e).
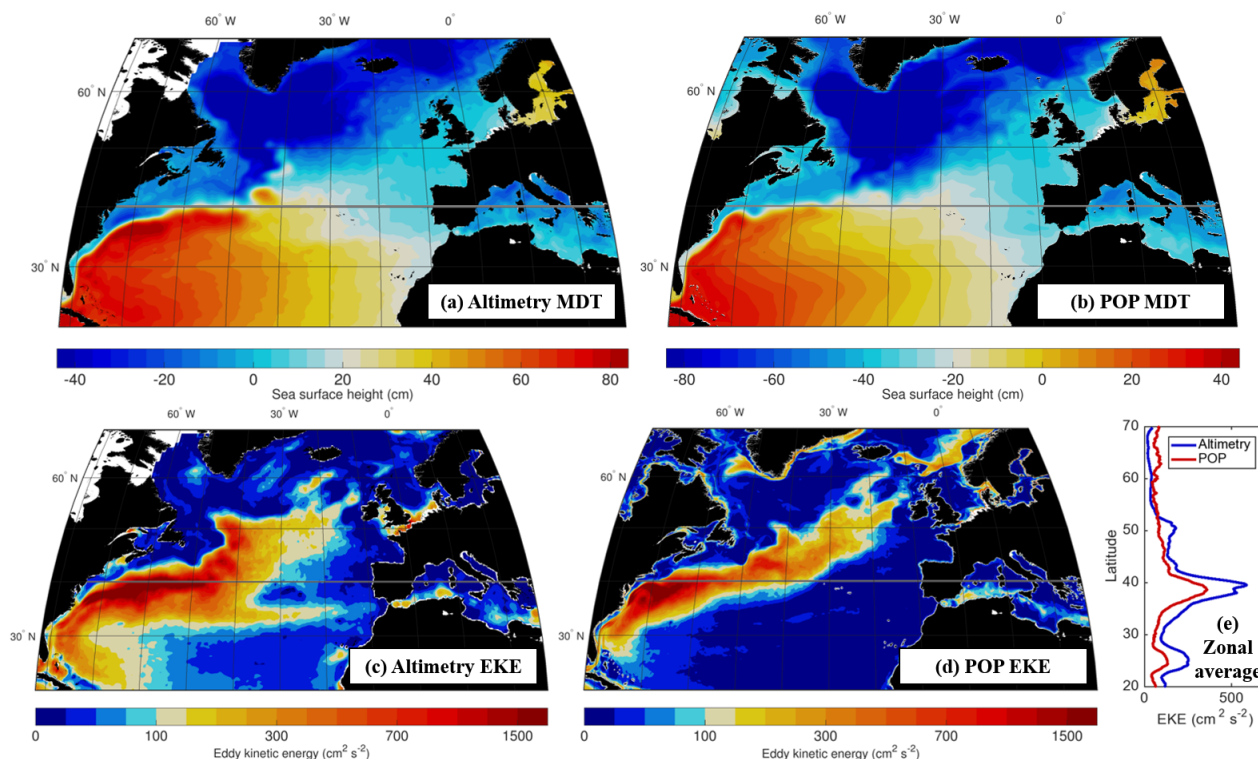
Figure 1. Comparison of mean dynamic topography from (a) CMEMS altimetry (1993-2016) and (b) POP simulation (1978-2009). The gray line indicates the 40°N latitude transect, the focus of this study. (c, d) Same as (c, d) but for surface eddy kinetic energy (EKE); POP sea surface height is low-pass filtered to remove variability at scales smaller than 0.5°, the Nyquist wavelength of the altimetry product. (e) Comparison of Atlantic zonally-averaged surface EKE from altimetry and POP.

2.2 Temperature flux decomposition

The meridional heat transport in the ocean is commonly regarded to consist of a mean and "eddy" component, where the "eddy" component is associated with velocity and temperature deviations from a temporal mean. Namely

$$\rho c_\rho \overline{vT} = \rho c_\rho \left(\overline{v}\,\overline{T} + \overline{v'T'} \right) \tag{1}$$

105   with ρ the reference density and c_ρ the specific heat capacity of seawater, and the meridional velocity and temperature are decomposed into time mean and deviation components $v = \overline{v} + v'$ and $T = \overline{T} + T'$ respectively. There are also cross-terms between the mean and deviation components in eq. (1), but these are zero by definition in time means. When the left-hand side is integrated zonally and vertically across a basin with zero net meridional flow ($\iint v\,dx\,dz = 0$), these heat fluxes are considered heat transports. The decomposition in eq. (1) is convenient for describing how much heat transport can be explained (and not

110   explained) by the ocean's mean state, but it provides little information about the processes actually responsible for the heat transport.

An alternative approach to the decomposition is to separate zonal mean and deviation components (e.g., Hall and Bryden, 1982); neglecting ρc_ρ to focus on the temperature flux, this decomposition is

$$\int vT\,dx = \int \left(\langle v \rangle \langle T \rangle + v''T'' \right) dx \tag{2}$$

115   where $\langle \rangle$ and $''$ indicate zonal mean and deviation respectively. While eq. (1) holds true only when the terms are time averaged, eq. (2) involves zonal integration or averaging, and therefore holds true without any time averaging. Since the term $\langle v \rangle \langle T \rangle$ varies in depth and time but not zonally, it quantifies the contribution to temperature transport from the overturning circulation, i.e., the meridional movement of warmer shallow waters over cooler deeper waters. The contributions of any lateral variations in the ocean are therefore contained in the $v''T''$ term. However, these lateral variations include a wide range of processes

120   that range in scale from subtropical and subpolar basin gyres, to instabilities at the smallest scales resolved by the model or observing system.

In order to separate the contribution of large-scale processes (e.g., gyres, long planetary waves) from mesoscale processes (e.g. transient and standing eddies), we introduce a further decomposition of the $v''T''$ term:

$$v''T'' = v_L T_L + \left[(v_L T_M + v_M T_L) + v_M T_M \right] \tag{3}$$

125   in which the subscripts $_L$ and $_M$ denote large-scale and mesoscale components of meridional velocity and temperature. The middle cross-terms on the right-hand side of eq. (3) are considered part of the mesoscale contribution since they would not exist without mesoscale processes; they are negligible when integrated or smoothed over a sufficiently large range in the interior, but near the boundaries the cross-terms may still make substantial contributions to basin-integrated transports. The separation

of large-scale and mesoscale components is carried out in the spectral (wavenumber) domain, with low-pass and high-pass

130 transfer functions such that given the Fourier wavenumber coefficients for (zonally-detrended) meridional velocity $V(k)$

$$V_L(k) = \left[0.5 + 0.5\,\mathrm{erf}\left(-s\,ln\frac{|k|}{k_0}\right)\right]V(k) \tag{4}$$

$$V_M(k) = \left[0.5 + 0.5\,\mathrm{erf}\left(s\,ln\frac{|k|}{k_0}\right)\right]V(k) \tag{5}$$

and analogously for the decomposition of temperature. It can be readily seen that the sum of eq. (4) and eq. (5) is the original

135 $V(k)$. After filtering, the zonal trends are added back to the large-scale velocity and temperature, but not the mesoscale velocity
and temperature. Since the POP grid is not aligned with lines of latitude in the North Atlantic, velocities and temperatures are
interpolated to regularly-spaced longitudes (0.1° interval) before the computation of eq. (4) and eq. (5) and then interpolated
back to the original model grid; this leads to a residual that is technically unassociated with either the large-scale or mesoscale,
though given that it results from interpolation errors it is likely more associated with the mesoscale. Meridional velocity outside

140 the basin boundaries and within interior land areas is set to zero; however, to minimize abrupt jumps in temperature and its
zonal derivative at the boundaries, a buffer is also included at the western and eastern boundaries after detrending but prior
to the application of the filters in eq. (4)–(5). Given x_b the western boundary position and x_c the zonal decorrelation scale
of temperature at a given latitude, depth, and time, the average values of temperature in the ranges $x_b < x < x_b + x_c$ and
$x_b + x_c < x < x_b + 2x_c$ (T_1 and T_2 respectively) are computed, and from these a boundary value $T_b = 1.5T_1 - 0.5T_2$ and slope

145 $T_s = (T_2 - T_1)/x_c$. Then an error function is fitted outside the boundary that approximates the slope of the temperature profile
approaching the western boundary

$$T''|_{x<x_b} = T_b\left\{1 + \mathrm{erf}\left[\frac{\sqrt{\pi}}{2}\left|\frac{T_s}{T_b}\right|(x - x_b)\right]\right\} \tag{6}$$

and the mirror opposite formulation is applied to the eastern boundary. For interior land areas, temperature is simply interpo-
lated across the land gap for the purposes of filtering.

150 There are two parameters in the transfer functions in eq. (4)–(5) that need to be chosen: s the steepness factor at the wave-
number cutoff, which is set to 5, and k_0 the cutoff wavenumber. To determine a sensible value for k_0 and the related cutoff
wavelength $\lambda_0 = 1/k_0$, spectral density estimates are computed from the POP meridional velocity v and temperature T fields at
40°N (Fig. 2). With high levels of mesoscale activity at 40°N, a clear mesoscale peak can be seen at wavenumbers correspon-
ding to wavelengths between 4° and 5° longitude (Fig. 2a); there is a similar peak in wavenumber spectra of the Gulf Stream

155 path through this region (e.g., Lee and Cornillon, 1996). The temperature spectral peak is less obvious, but is still visible rela-
tive to the general downward slope with increasing wavenumber (Fig. 2b). Wavelengths corresponding to the mesoscale peak
and large-scale/mesoscale transition were identified by smoothing the spectral density curves for v and T in logarithmic space
and identifying the minimum and maximum of $\partial^2(\ln V)/\partial(\ln k)^2$ within broad expected ranges (2°-20° wavelengths for the
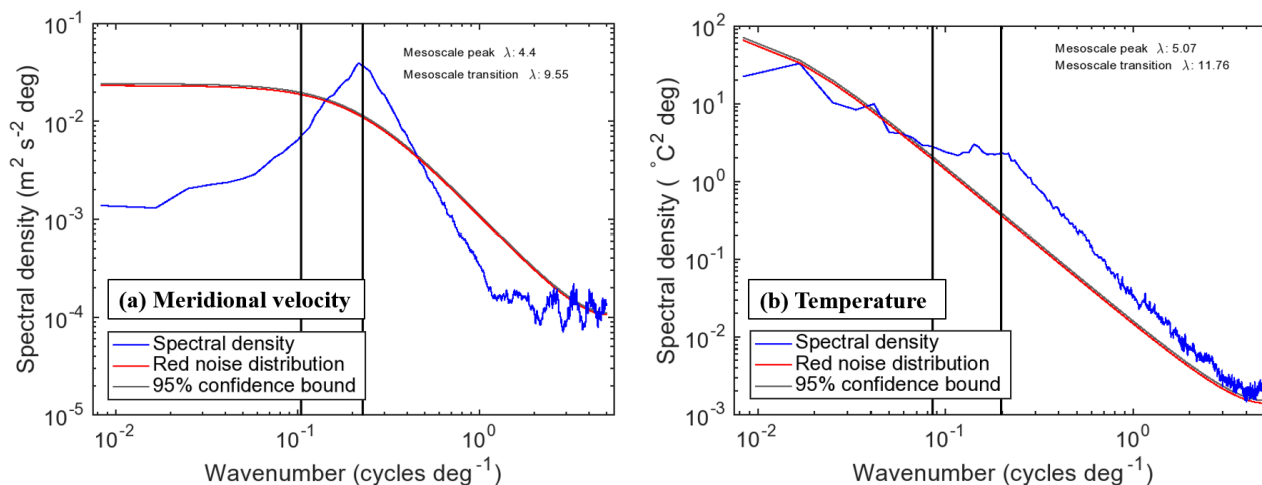
Figure 2. Zonal wavenumber spectral density estimate of (a) meridional velocity and (b) temperature in the Atlantic at 40°N from POP. The vertical lines and text indicate the wavelength (in degrees) of the mesoscale transition and peak as calculated from each spectral estimate, based on the logarithmically-smoothed spectral profile. The red and gray curves indicate the red noise distribution expected from lag-1 (model grid-scale) autocorrelation and the corresponding 95% upper confidence bound.

mesoscale peak, 3°-30° wavelengths for the large-scale/mesoscale transition). Though computed independently, wavelengths

160   for the mesoscale peak and transition identified from the spectral curves of v and T are similar, providing confidence that the mesoscale signal starts to emerge at wavelengths shorter than 10° and peaks at approximately 5°. Though a 5° wavelength is much longer than the first baroclinic Rossby radius (∼20 km at this latitude), it does compare favorably with eddy radii of approximately 100 km observed at 40°N in altimetry data (Chelton et al., 2011); the peak wavelength is expected to be approximately 4 times the typical eddy radius. Hence to obtain an optimal separation between mesoscale and large-scale processes,

165   the cutoff wavenumber in eq. (4) and (5) is set to k_0 = 1/10 cycles/°, corresponding to a 10° wavelength.

Applying this procedure, the contributions of the overturning, large-scale, and mesoscale components to heat transport can be computed for a range of latitudes in the North Atlantic (Fig. 3), along with the residual error that results from the interpolation to and from the regularly-spaced longitude grid. The time mean contribution to heat transport in the tropical North Atlantic is approximately 0.8 PW (Fig. 3a), which is weaker than observational (Johns et al., 2011) and model-based (e.g., Tréguier et al.,

170   2012) estimates. The weaker Atlantic MHT in POP is likely associated with a weaker meridional overturning circulation of 12-13 Sv, which is towards the low end of model estimates (8–28 Sv, e.g., Danabasoglu et al., 2014). Despite the probable low bias in the strength of the overturning, the overturning contribution to time mean heat transport is much larger than non-overturning components at low latitudes (Fig. 3a), in agreement with earlier findings (Bryan, 1982; Johns et al., 2011). Moving northward, the overturning contribution steadily decreases while the mesoscale contribution increases, reaching peaks at 39°N and again

175   at 45°N. The time mean mesoscale contribution is larger than the contribution of large-scale (non-overturning) processes in the

range 39°-46°N, while to the north and south large-scale processes contribute more, likely driven by the strong subpolar and subtropical gyre circulations respectively. The residual contribution is negligible at all latitudes in the North Atlantic, implying that interpolation errors do not impact our assessment of contributions to time mean MHT.
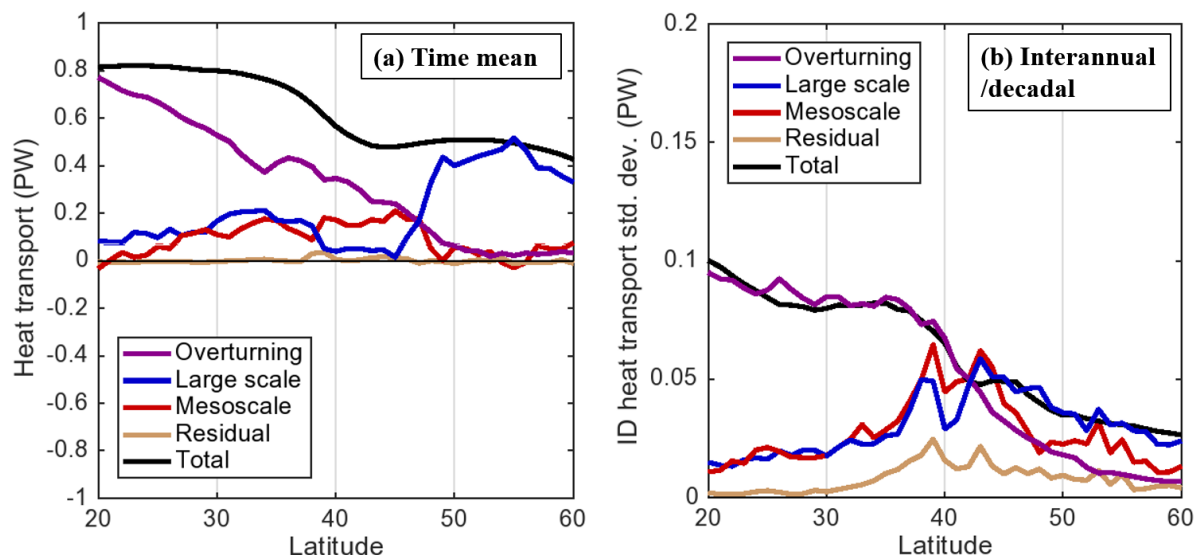
Figure 3. (a) POP time mean contributions to meridional heat transport (MHT) in the North Atlantic from overturning, large-scale, and mesoscale components, and the unexplained residual, as a function of latitude. (b) Standard deviation (on interannual/decadal timescales) of the components of MHT.

The flux components have also been filtered to consider their contribution to interannual and decadal (ID) variability, by
180   removing the seasonal cycle and applying a low-pass filter with a cutoff period of 14 months (Fig. 3b). In the North Atlantic overall, the large-scale contribution to ID variability remains comparable to the mesoscale contribution, except at 39°–41°N (where the mesoscale is larger) and poleward of 44°N (where the large-scale is larger). The residual's contribution to ID variability is relatively small, if not as negligible as its contribution to time mean MHT. In the rest of the analysis, we focus on 40°N to highlight how the spatial-scale decomposition can help diagnose the mechanisms of temperature flux variability across
185   a transect. The 40°N latitude is an ideal location for this analysis, as the mesoscale contributions to time-mean and interannual/decadal (ID) MHT are both substantial, and higher than large-scale contributions at the same latitude (Fig. 3). Though the overturning contributions are still larger than the mesoscale at 40° N, we will disregard the overturning contributions in the remainder of this study to focus on the novel large-scale/mesoscale decomposition.

3 Variability and cross-basin structure of temperature fluxes

190 3.1 Time series of ID variability
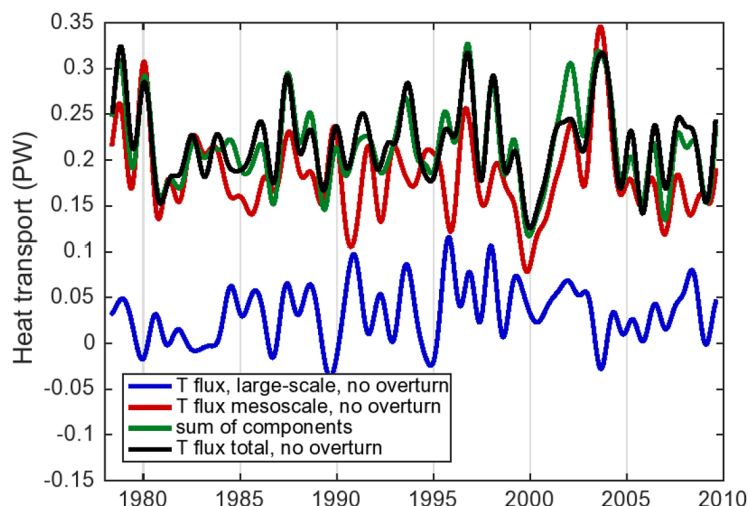
Figure 4. Basin-integrated contributions of large-scale and mesoscale v and T to the ID variability of heat transport across 40°N in the Atlantic. The zonal means of v and T are removed prior to the computations. The sum of the large-scale and mesoscale components (green) is compared to the total temperature flux minus the overturning contribution (black); differences between the two are due to filter behavior at the boundaries.

With the overturning contribution removed, the time series of the large-scale and mesoscale temperature flux components eq. (3) at 40°N (Fig. 4) confirms that both the time mean and ID variability of the mesoscale temperature flux (MTF, red curve) are larger than the large-scale temperature flux (LTF, blue curve). The LTF is not negligible however, and some peaks in the total non-overturning temperature flux (black curve) such as those in 1993 and 2008 can be attributed to the LTF more than the

195   MTF. At some times the LTF and MTF are anticorrelated and effectively cancel each other out (1990, 1995), and at other times both fluxes contribute substantially to a temperature flux peak (1979, 1987). Yet several of the highest peaks in the total flux (1980, 1996, 2003) are associated only with MTF variability, and the lowest total flux in the entire series (beginning of 2000) is also a result of low MTF. The sum of the two components (LTF and MTF) agrees very well with the total non-overturning temperature flux, implying a small residual and suggesting the overall validity of the LTF and MTF components. The only

200   exception is in 2002 where the effect of interpolation errors likely results in one or both components being too high.
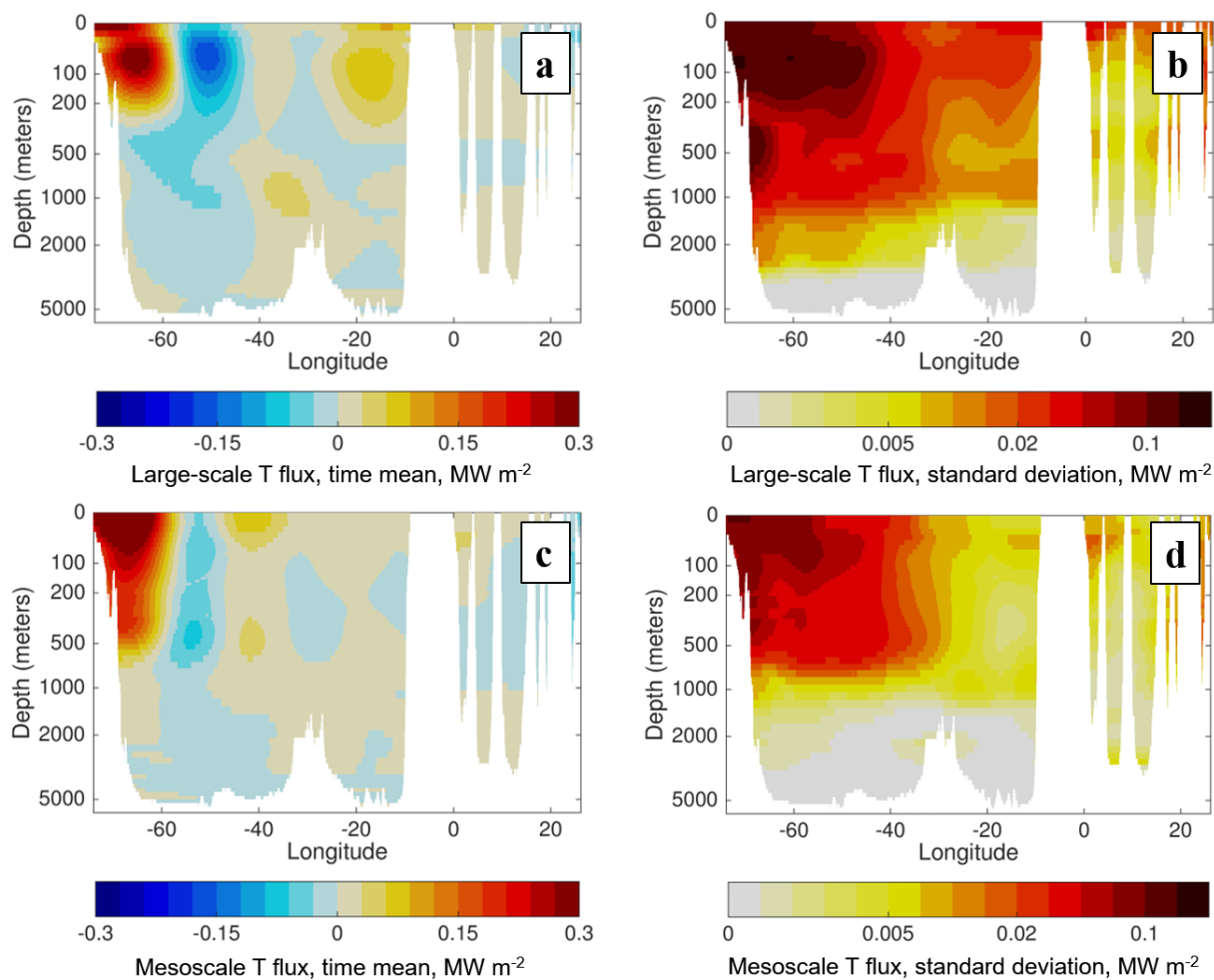
Figure 5. (a) Time mean and (b) ID standard deviation of the zonally-smoothed large-scale temperature flux. Zonal smoother is a low-pass filter for wavelengths longer than 20° longitude. (c, d) Same as (a, b), but for the zonally-smoothed mesoscale temperature flux.

3.2 Cross-basin structure of flux components

We now turn our attention to the parts of the transect that contribute most to the time mean and ID variability of the large-scale and mesoscale temperature fluxes. The time-mean LTF is the result of three areas of contribution in the upper ocean (<300 meters), as well as two areas at depths of 400-1200 meters (Fig. 5a). The upper ocean contributions to time-mean LTF are mostly found near the western boundary, where a positive LTF closest to the boundary is partially compensated by negative LTF further offshore near 50°W. A more modest positive LTF contribution is also located near the eastern boundary of the main ocean basin (20°-10°W). The 400–1200 meter contributions are between the western boundary and the Mid-Atlantic

Ridge. These contributions of negative LTF at 65°-45°W and positive LTF near the Mid-Atlantic Ridge are more substantial

than they may appear in Fig. 5a, since they span a larger depth range (note the logarithmic depth scale of the figure). Integrated

210 in depth, the deep LTF contributions are comparable to the shallow eastern boundary contribution, and their contribution to ID

variability is higher than the shallow eastern boundary, if not as high as the shallow western boundary (Fig. 5b). The time mean

MTF structure is simpler to interpret than the LTF, as it is vertically coherent and mostly confined to the upper 700 meters

(Fig. 5c). An area of positive MTF near the western boundary is stronger than the co-located positive LTF, the negative MTF

at 60°-50°W is weaker than its LTF counterpart, and there is an additional modest area of positive MTF near 40°W. The ID

215 variability of the MTF is also confined almost entirely to the upper 700 meters, and west of the Mid-Atlantic Ridge (Fig. 5d).
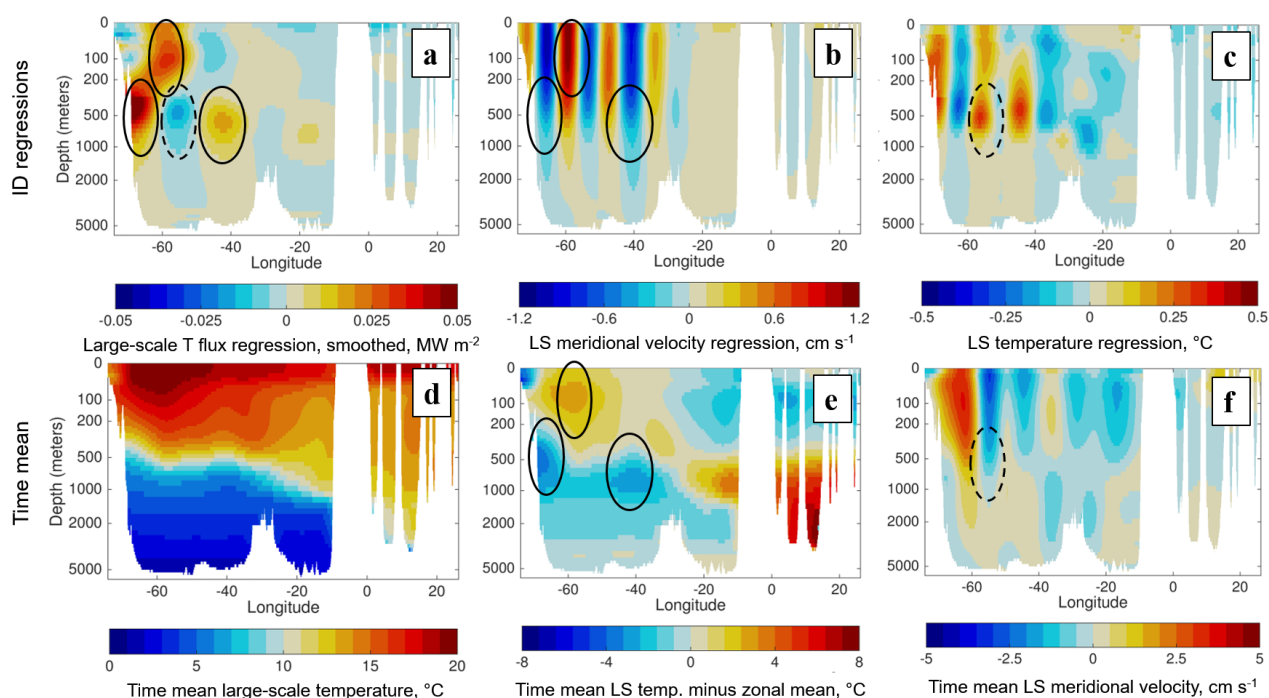
Figure 6. Components of the large-scale temperature flux variability. (a) Regression of $+1\sigma$ of the basin-integrated large-scale (LS) temperature flux onto the local zonally-smoothed large-scale (LS) temperature flux, and onto (b) LS meridional velocity and (c) LS temperature. (d-f) Time mean structure of LS temperature (d) with zonal mean and (e) without zonal mean, and (f) time mean LS velocity structure. Solid and dashed ellipses indicate contributions from the $v'_L \overline{T_L}$ and $\overline{v_L} T'_L$ components respectively.

The ID variability of the LTF can be explained in terms of the structure of its large-scale velocity and temperature constituents

(Fig. 6). Using linear regression, we assess the local contributions of the LTF associated with a $+1\sigma$ (1 standard deviation above

the mean) basin-integrated LTF (Fig. 6a). Here the LTF is zonally-smoothed with a cutoff wavelength of 20°, to facilitate

interpretation and reduce the appearance of zonal LTF variability at wavenumbers up to twice that of the individual velocity

220 and temperature constituents. The regression of the basin-integrated onto local LTF reveals a substantial influence of variability

at 300-1000 meters depth. Of the three main areas of contribution (positive regression values, indicated by solid ellipses), two are in this depth range in the lower thermocline, with water temperatures of 5°-12°C (Fig. 6d). In this depth range the coldest waters are found at the western boundary, and the LTF contribution increases when the flow is southward (Fig. 6b), as the boundary temperature is cold relative to the zonal mean (Fig. 6e). Hence the contributions peak near the western boundary

225 and at 40°W (Fig. 6a) where there is a local minimum in temperature (Fig. 6e). The third area of contribution to the LTF is associated with the near-surface maximum in temperature (Fig. 6e), and here northward flow increases the LTF. All of these contributions are associated with velocity variability advecting time-mean temperature structure ($v'_L \overline{T_L}$). The time mean velocity field does also advect temperature variability ($\overline{v_L} T'_L$), though the main contribution from this term (Fig. 6a; dashed ellipse) is anticorrelated with the basin-integrated variability, and therefore acts to compensate the other contributions. This

230 compensation occurs in the region of time-mean southward flow near 55°W (Fig. 6f), where warmer flow (Fig. 6c) will cause the total LTF to be more negative.

The structure of MTF variability on ID timescales (Fig. 7a) is similar to the structure of the time-mean MTF; however, the interior region (50°-35°W) which had a modest positive time-mean MTF becomes more important for ID variability. The focus of this interior MTF is also deeper than the boundary MTF, near 500 meters depth where the thermocline shoals (Fig.

235 6d). The western boundary remains significant for MTF variability; the middle region (60°-50°W, where there is negative time-mean MTF) may have a compensating effect, but its magnitude is small compared to the western boundary and interior MTF contributions (Fig. 7a). It is worth noting that the structure of MTF variability is very similar to the deeper LTF variability contributions (Fig. 6a), but the MTF contributions occur shallower than the LTF contributions and extend to the surface. The similarity might result from a direct interaction between deep velocities and mesoscale eddies, or the large-scale current and

240 temperature structure influencing both LTF and MTF variability. Given the predominance of transient, propagating features in the oceanic mesoscale (e.g., eddies), most ID MTF variability is not associated with the time-variable advection of time mean $\overline{T_M}$, but with the rectification of intraseasonal v'_M and T'_M variability onto ID timescales. Therefore, the regression method used to explain the sources of LTF variability in Fig. 6 is insufficient to explain sources of the MTF, and different diagnostics are needed.

245 Figure 7a implies that two regions (a boundary and interior region) should account for most MTF variability on ID timescales. Time series of the MTF in each of these regions (Fig. 7b) confirm this while also illustrating differences in the timescales of variability present in each region. The variability of MTF in the boundary region (70°-60°W) predominantly occurs on higher-frequency interannual timescales with peaks every 1–4 years, and many of these peaks are aligned with the basin-integrated MTF. The interior region (50°-35°W) has some interannual variability, but there also appears to be an underlying decadal

250 signal, and elevated interior MTF peaks in 1980 and 2003 align with the two highest values of basin-integrated MTF during this period. The time-mean discrepancy of ∼0.07 PW between the sum of the components (green dashed curve) and the basin-integrated total (black curve) is mostly the result of the zonal smoothing, which allows the MTF variability from each region to be better represented but leaks some temperature flux at the boundaries.
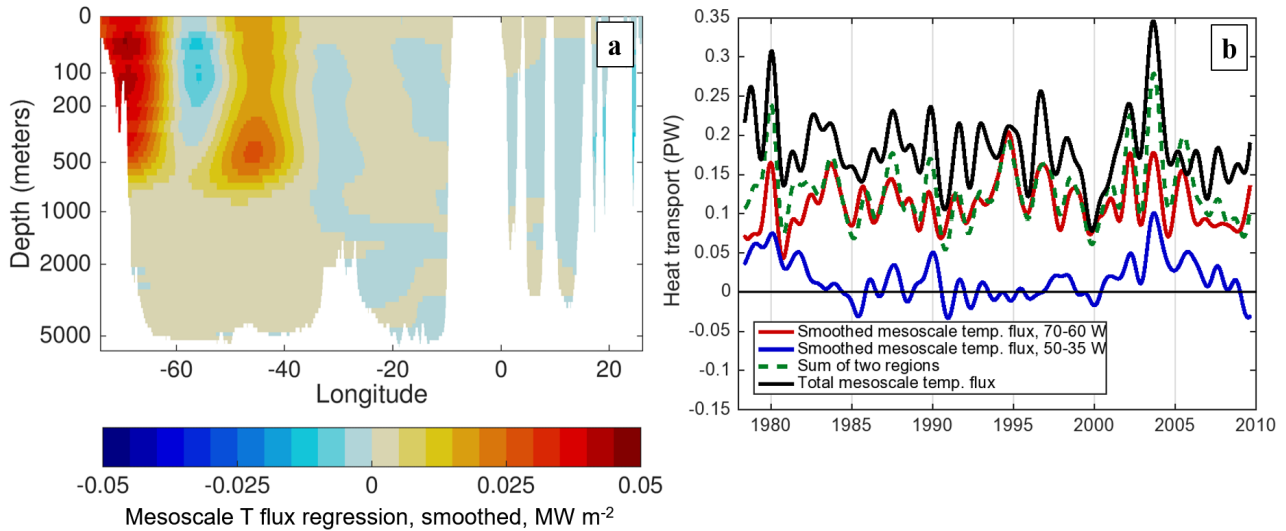
Figure 7. (a) Regression of $+1\sigma$ of the basin-integrated mesoscale temperature flux onto the local zonally-smoothed mesoscale temperature flux, indicating the distribution of the temperature flux contributions along the transect. (b) Time series comparison of the zonally-smoothed mesoscale temperature flux integrated in two regions (70–60° W and 50–35° W) and the sum of the contributions in these regions with the total basin-integrated mesoscale temperature flux.

4 Drivers of MTF variability

255 ### 4.1 EKE variability and MTF

The eddy kinetic energy or EKE (defined as half the variance of the velocity vector with the time mean removed) is generally considered to be an indicator of the level of mesoscale activity in a given location and time; hence we expect that EKE might influence MTF variability. This relationship can be expressed (e.g., Holloway, 1986; Stammer, 1998) as

$$v_M T_M = \kappa \frac{\partial T}{\partial y} \propto \sqrt{\overline{v'^2}} L_{\mathrm{mix}} \left(-\frac{\partial T}{\partial y} \right) \qquad (7)$$

260 where L_{mix} is a mixing length parameter that is related to the width of the local frontal zone associated with the meridional temperature gradient (Green, 1970). Assuming fairly isotropic velocity variability

$$v_M T_M \propto \sqrt{\mathrm{EKE}} L_{\mathrm{mix}} \left(-\frac{\partial T}{\partial y} \right) \qquad (8)$$

It would be convenient if EKE (specifically surface EKE) was the primary influence on MTF variability, since this can be diagnosed from satellite altimeters and would allow direct observational estimates of MTF variability. However, at 40°N

265 surface EKE variability is not a reliable indicator of time variations in the MTF (Fig. 8). High MTF occurs at times of at
least moderately high transect-averaged EKE, and significant MTF peaks are all associated with surface EKE peaks. However,
many of the highest values of surface EKE (1985-86, 1992, 2008) do not seem to drive an increased MTF; therefore, elevated
EKE seems to be a necessary but not sufficient condition for high MTF along this transect. Local correlations of surface EKE
and MTF in the eddy-active western part of the basin (not shown) are at best marginally significant at 95% confidence levels,
270 further suggesting that high levels of mesoscale energy do not imply elevated MTF.
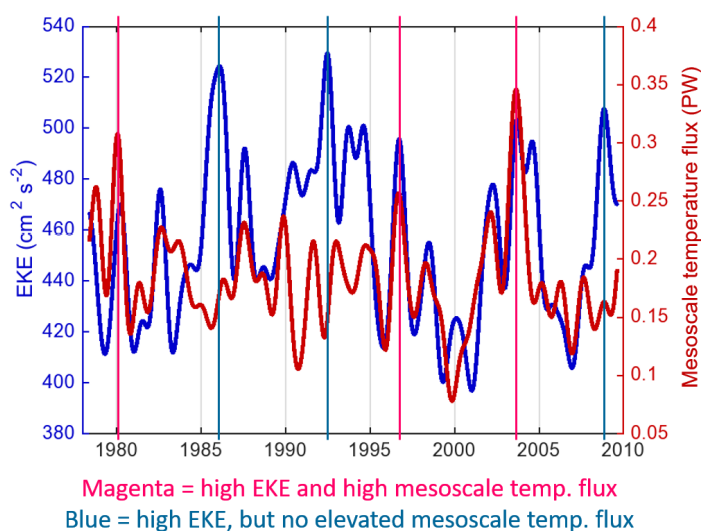
Figure 8. Comparison of the basin-integrated mesoscale temperature flux (red) with the zonally-averaged surface eddy kinetic energy (EKE)
along 40°N.

4.2 Constituents of MTF variability

To focus on what conditions permit high MTF across 40°N, we consider the three highest peaks in the MTF time series, in
1980, 1996, and 2003 (Fig. 8). The spatial structure of MTF variations indicates that all of these peaks were associated with
higher than usual MTF values in more than one region (Fig. 9a,b). In 1980 and 2003 (the two highest peaks) the elevated MTF
275 contributions clearly originate in the boundary and interior regions. In 1996, a positive MTF anomaly in the boundary region
is supplemented by a positive anomaly in the adjacent 60°-50°W (Fig. 9b), which corresponds to an abatement of the usually
negative MTF in this region (Fig. 9a). Other positive anomalies in the 60°-50°W do not seem to influence basin-integrated
MTF variability however (Fig. 9c), so 1996 may be an unusual episode.
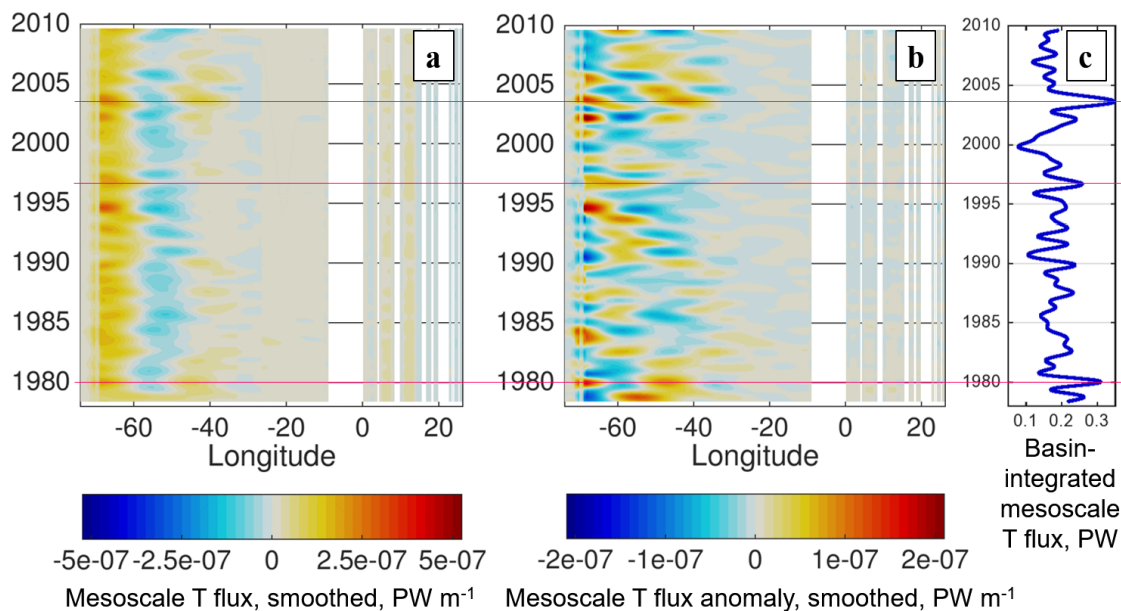
Figure 9. (a) Hovmöller diagrams of the zonally-smoothed mesoscale temperature flux at 40°N. (b) Same as (a) with the time mean removed. (c) Time series of the full basin-integrated mesoscale temperature flux. Magenta lines indicate the times of highest mesoscale contribution to meridional heat transport.

In addition to the proportionality relationship in eq. (8), the MTF can be decomposed in terms of the contribution of the amplitude and co-variability of v_M and T_M

$$v_M T_M = \sigma_{v_M} \sigma_{T_M} R \tag{9}$$

where σ_{v_M} and σ_{T_M} are the standard deviations of v_M and T_M and R is the correlation coefficient of v_M and T_M; the standard deviations and correlations are computed in windows that are localized in space and time to study spatiotemporal variability. In relation to eq. (8), EKE is most likely to influence σ_{v_M}, while the meridional temperature gradient $\partial T/\partial y$ will likely influence σ_{T_M} and potentially R. By computing the constituents on the right-hand side of eq. (9) in moving windows spanning 10° longitude and 1 year ranges (in the upper 1000 meters), the contributions of each constituent to MTF variability are evident (Fig. 10a-c). The basin-integrated MTF is the result almost entirely of fluxes west of the Mid-Atlantic Ridge (∼30°W) because σ_{v_M} and σ_{T_M} are much larger in the western part of the basin than in the east (Fig. 10a-b). However, R is responsible for the time-mean structure of the MTF within the western part of the basin; in fact, R is typically negative between 60°-50°W despite the fact that the large-scale meridional temperature gradient has the same sign here as elsewhere (Fig. 10d), implying an upgradient diffusivity of temperature at 60°-50°W.
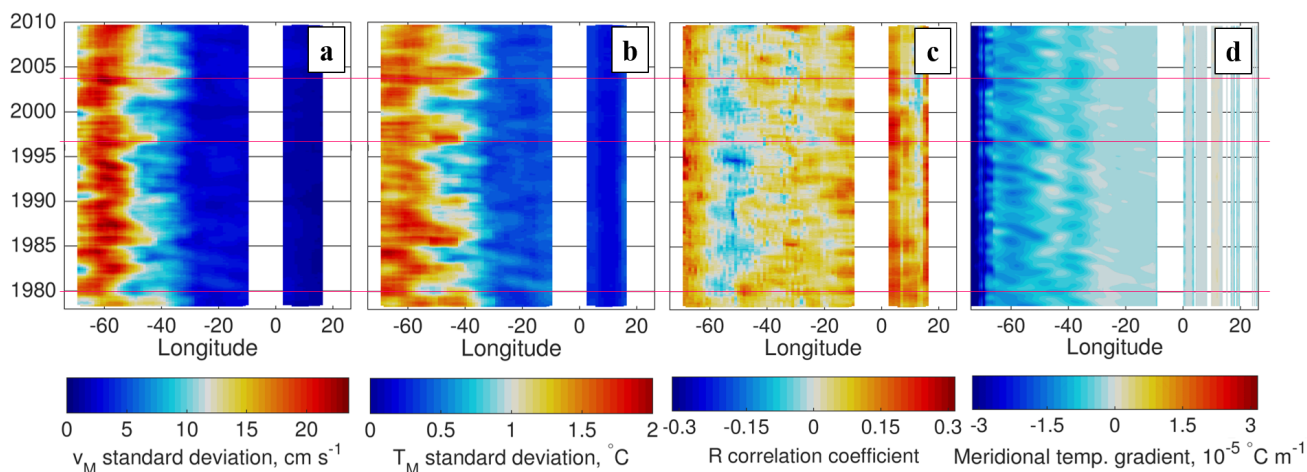
Figure 10. (a-c) Breakdown of mesoscale temperature flux according to the decomposition $v_M T_M = \sigma_{v_M} \sigma_{T_M} R$, where σ_{v_M} and σ_{T_M} are the local standard deviations of mesoscale v and T, and R is the local correlation coefficient between them. Standard deviations and correlations are computed for the upper 1000 m of the ocean, in moving windows spanning $10°$ longitude and 1 year. (d) Meridional temperature gradient, determined using a regression fit between latitudes $38°$ N and $42°$ N and zonally and temporally low-pass filtered with $10°$ and 14 month thresholds respectively.

When the time means are removed from the constituents in eq. (9), the sources of MTF variability can be attributed more clearly (Fig. 11). In 1980, high MTF is driven by a strongly positive R anomaly, coincident with a steeper-than-usual temperature gradient in the interior region (Fig. 11c,d). By contrast, high MTF in 1996 is supported by slight positive anomalies in σ_{v_M}

295 and R (and possibly σ_{T_M}), while in 2003 has more robust positive anomalies in all of these contributions. The anomalies also suggest a difference in behavior between the boundary and interior regions: the MTF is more responsive to σ_{v_M} (and likely EKE) variations west of $50°$W where time-mean σ_{v_M} is larger, while in the interior an increase in σ_{T_M} and/or R is necessary to increase MTF. Lastly, all three peak events (Fig. 9) are associated with an anomalously steep meridional temperature gradient in their source regions (Fig. 11d). Just as importantly, there was no robust positive (weaker) gradient anomaly during these

300 three events, in contrast with 1990-95 when weaker gradients in the interior region may have contributed to negative (weak) anomalies in all three constituents.

4.3 Large-scale temperature flux contributions

Having identified the influence of the meridional temperature gradient on MTF variability, we consider the role of the large-scale current and temperature in generating anomalous meridional temperature gradients. The path of the Gulf Stream extension

305 sets the location of strong temperature fronts in the western Atlantic at this latitude; notably, its path during high MTF events tends to be further north than usual at $\sim 66°$W (Fig. 12a). This location is important because in the POP simulation it is where the mean path of the Gulf Stream first approaches $40°$N. When there is a northward shift in the path at this region, the Gulf
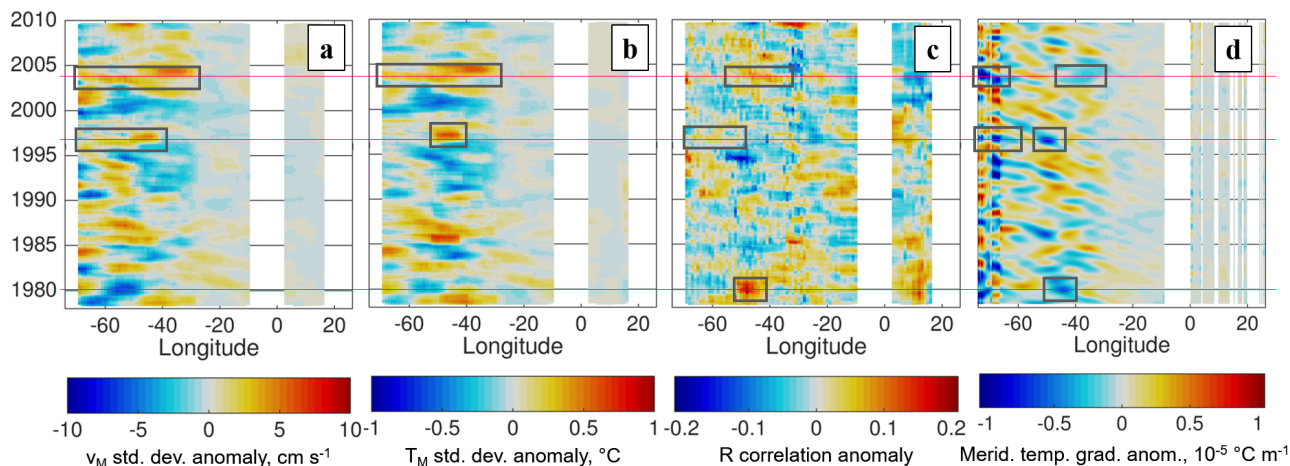
Figure 11. Same as Fig. 10, but with the time means removed. Anomalies associated with peak MTF events are indicated by gray boxes.

Stream's crossing of 40°N can happen hundreds of kilometers west of the usual location, and the meridional temperature gradient is steeper west of 65°W (Fig. 10d). Large-scale temperature anomalies in the upper ocean also show a difference in

310 the mechanism for meridional temperature gradient anomalies at the boundary vs. the interior (Fig. 12b-d). When the boundary region contributes significantly to high MTF (1996 and 2003), the steeper temperature gradient is associated with a positive temperature anomaly south of 40°N. When the interior region contributes to high MTF (1979-80 and 2003), the steeper gradient is associated with a negative temperature anomaly north of 40°N. Since the mean path of the Gulf Stream is just south (north) of 40°N in the boundary (interior) region, each of these temperature anomaly patterns would nudge the path of the Gulf Stream

315 closer to 40°N, intensifying the temperature gradient across the transect.

The importance of the meridional temperature gradients in both the boundary and interior regions is emphasized when comparing the time series of the gradients to the MTF in each region (Fig. 13). In particular, the higher-frequency interannual variability in MTF in the boundary region is closely associated with variations in the meridional temperature gradient (Fig. 13a). In the interior region, decadal variability is not as pronounced in the meridional temperature gradient as it is in the MTF;

320 there are a number of times when the meridional temperature gradient is steeper than the average, without a major effect on MTF (Fig. 13b). However, two of the most significant maxima in meridional temperature gradient (1980 and 2003-04) are associated with elevated MTF, so steeper gradients at least make significant positive MTF events more likely.
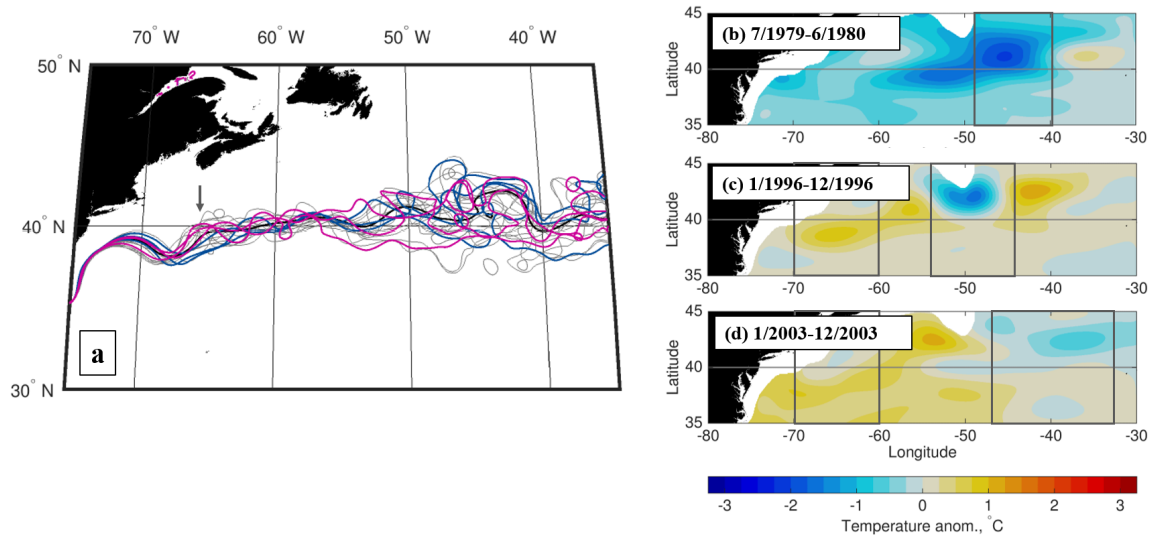
Figure 12. (a) Spaghetti plot showing annual averages of the -20 cm contour path (approximate Gulf Stream path) in POP; magenta lines indicate the path during times of high EKE and MTF, blue lines indicate times of high EKE but low MTF, and gray lines are randomly distributed 1-year periods during 1978–2009. The arrow indicates a path anomaly associated with the high MTF events. (b-d) Large-scale temperature anomalies, averaged 0–1000 meters, during the periods of high mesoscale temperature flux. The gray boxes indicate the region(s) in which negative meridional temperature gradients contribute the most to the mesoscale temperature flux.
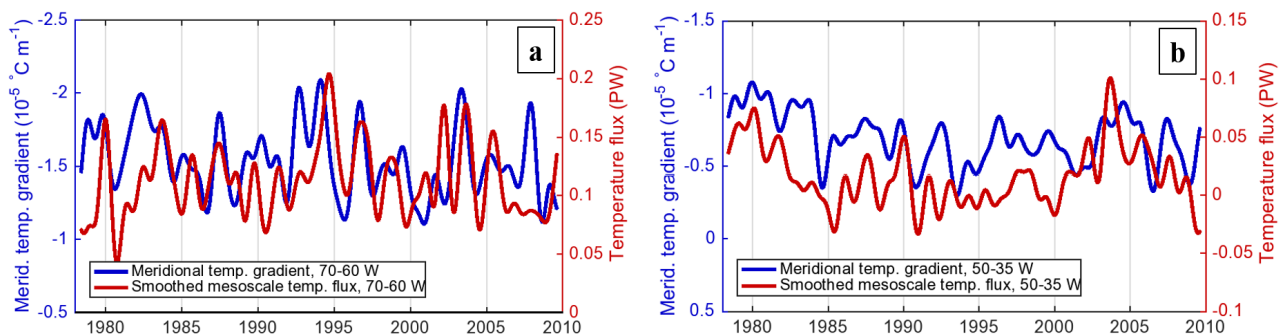
Figure 13. (a) Time series comparison of 0–1000 m meridional temperature gradient averaged along the 40° N transect between 70° W and 60° W (boundary region), with the zonally-smoothed mesoscale temperature flux integrated in the same region. The y-axis of the meridional temperature gradient is inverted to align its orientation with the MTF. (b) Same as (a), but in the interior region (50°-35° W).

5   Discussion

5.1   Novel aspects of this study

325   A novel aspect of this study is the spatial decomposition method to separate the mesoscale and large-scale contributions to MHT, in contrast to the use of temporal co-variability of velocity and temperature in many previous studies. As a diagnostic tool, the spatial-scale decomposition of MHT has important advantages over the more common approach of separating time mean and time deviation (often called "eddy") fluxes. The mechanisms that drive large-scale processes such as gyres (wind forcing, boundary/topographic constraints) are typically distinct from those driving mesoscale processes (e.g., baroclinic and

330   barotropic instability); quantifying the spatial scales of MHT contributions and their distribution is a first step towards understanding the processes that contribute to MHT. Moreover, rather than being defined relative to a time mean over an arbitrary time period (e.g., the post-spinup time span of the model simulation), the mesoscale and large-scale contributions are physically meaningful at each timestep, so long as they are basin-integrated across transects with a net volume flux near zero.

This study also outlined an approach for diagnosing the geographical origins of LTF and MTF variability. Large-scale

335   temperature fluxes can generally be explained in terms of large-scale velocity and temperature components directly, with at least one time mean component involved (Figure 6). Mesoscale processes such as transient eddies produce rectified fluxes at spatial (and temporal) scales that are much larger (longer) than the original velocity and temperature anomalies. However, using spatial smoothing the MTF can be traced to specific locations (Fig. 5b,7), and supplemented by an analysis of the conditions that influence the MTF and instability in those regions (Fig. 8–12).

340   In our analysis of MTF variability at 40° N, we found that the influence of the meridional temperature gradient is modulated by the velocity-temperature correlation, whose importance is emphasized by Fig. 10–11. In addition to its role in driving MTF temporal variability, the correlation explains the negative time-mean temperature flux at 60°-50° W, indicating that there is an upgradient flux across the (still-negative) meridional temperature gradient (Fig. 10c,d). Other studies of mesoscale eddy characteristics and heat fluxes (e.g., Hausmann and Czaja, 2012; Gaube et al., 2015; Frenger et al., 2015; Tréguier et al., 2017)

345   have considered the displacement of temperature relative to velocity/pressure anomalies in eddies. Yet this work illustrates the impact of even subtle changes (of order 0.1) in the velocity-temperature correlation coefficient; hence more comprehensive studies of the velocity-temperature correlation, its dependence on the structure of nearby fronts and relationship to existing theories of diffusivity are needed.

5.2   Comparison of MTF with previous formulations of the eddy flux

350   It is helpful to compare how the mesoscale MHT we estimated compares to those based on previous methods, i.e., the co-variability of velocity and temperature (1) for all time scales ("time-varying"; e.g., Jayne and Marotzke, 2002; Tréguier et al., 2017) and (2) for deviations from 3 month-averages only ("high frequency"; Volkov et al., 2008). Because of the differences in models (including resolution and parameterization), a direct comparison of mesoscale MHT in our studies with "eddy" heat transports from these previous studies is not suitable. We therefore compare our mesoscale MHT with the "eddy" MHT

355   based on previous methods using the same POP model output (Fig. 14). The time-varying $v'T'$ term happens to be a decent
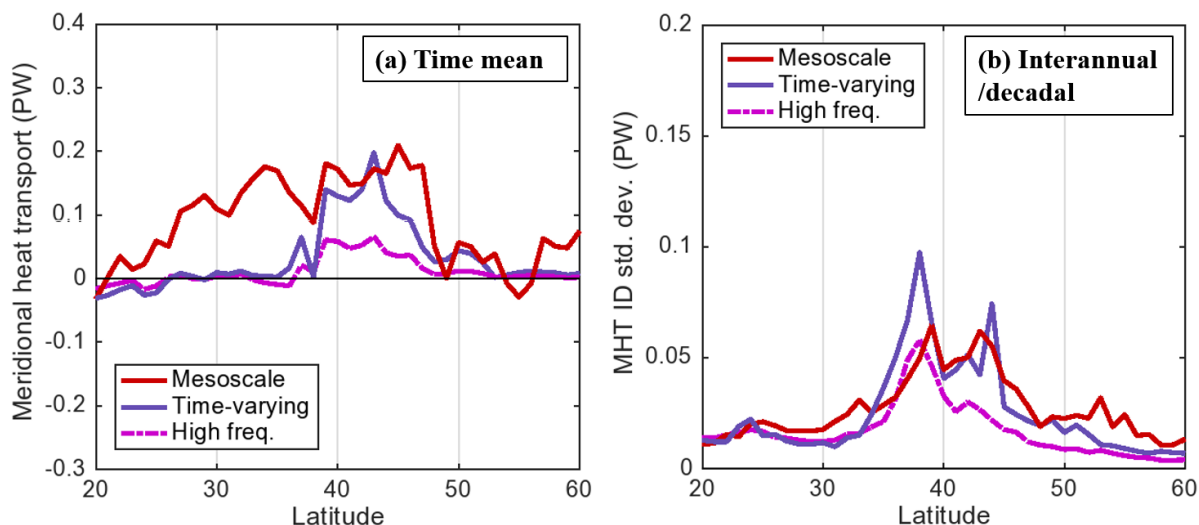
Figure 14. (a) POP time mean contributions to meridional heat transport (MHT) in the North Atlantic from "eddy" formulations computed three ways: the "mesoscale" component computed as the bracketed portion of eq. (3), the "time-varying" component $v'T'$ (e.g., Jayne and Marotzke, 2002), and the "high frequency" component using only v' and T' on timescales shorter than 3 months (Volkov et al., 2008). (b) MHT standard deviation (on ID timescales) of the three "eddy" formulations.

approximation of the mesoscale contribution to the time mean MHT in the 39°–44°N latitude range (Fig. 14a), corresponding to the region just north of the Gulf Stream separation. However, south of the Gulf Stream separation a substantial mesoscale contribution (0.1–0.2 PW) to time mean MHT is not represented at all in the time-varying contribution. This difference can be attributed to stationary mesoscale structure near the western boundary, specifically the narrow northward jet of the Gulf Stream

360 (width 1°–1.5° longitude) and the tight southward recirculation just to the east (width 2°–4° longitude). These features are not considered part of the traditional "eddy" flux formulation, yet they can only be accurately simulated in model simulations (and observational sampling) that resolves the mesoscale.

Regarding the timescales of rectified contributions to time-mean MHT, intraseasonal (high) frequencies account for about 30–40% of the total time-varying contribution in the active eddy region north of the Gulf Stream separation (Fig. 14a). While

365 mesoscale eddies are typically associated with intraseasonal frequencies, in the strong eastward flow of the Gulf Stream the westward propagation of eddies and meanders is slowed and even in some cases reversed, resulting in more low-frequency (and stationary) mesoscale variability driving MHT. Regarding ID variability, the mesoscale and time-varying MHT also have contributions of comparable magnitude in the 39°–44° N range, though with substantive differences at 38° N near the Gulf Stream separation and north of 50° N (Fig. 14b).

6 Conclusions

In this study a new decomposition method has been used to distinguish the contributions of mesoscale vs. larger-scale processes to meridional heat transport in the North Atlantic by using spatial scales (rather than temporal deviations) of velocity and temperature. This analysis technique can be applied to eddy-permitting ocean and coupled GCMs to better quantify the temperature flux produced by mesoscale ocean processes in the model. Applying this spatial-scale decomposition method in the North Atlantic, a substantial mesoscale contribution to time-mean, non-overturning MHT was found in the 32°–47° N latitude range that exceeded the large-scale non-overturning contribution, while somewhat less than the overturning contribution (Fig. 3a). North of the Gulf Stream separation the mesoscale contribution is associated with time-variable fluxes and so it is similar to the contribution of the traditional "eddy" temperature flux (Fig. 14a). However, south of the Gulf Stream separation there is a substantial mesoscale contribution to time mean MHT where the traditional "eddy" temperature flux is negligible, since stationary (not time-variable) mesoscale processes drive most of the MHT at these latitudes. Since the mixing effects of mesoscale processes apply to both stationary and time-variable processes, the mesoscale temperature flux is a more meaningful estimate of the mesoscale contribution to MHT that should be represented by eddy parameterizations in non-eddying models (e.g., Gent and McWilliams, 1990).

This study has also considered the relationship of mesoscale temperature flux variability to variations of indicators such as the EKE and meridional temperature gradient. The first unexpected result is that eddy kinetic energy (or at least surface EKE) is not a reliable indicator of MTF variability, with most of the highest instances of zonally-averaged surface EKE not being associated with an elevation in the MTF (Fig. 8). It is not surprising that meridional temperature gradients influence MTF variability, given that cross-frontal gradients are a part of classic theories of diffusivity and lateral mixing dating back at least to Taylor (1915). Yet the low magnitudes of the velocity-temperature correlation R imply that even small changes in R can have a large impact proportionally on the MTF. Hence an improved understanding of velocity and temperature structure within mesoscale features is necessary to inform accurate representations of meridional temperature fluxes in models.

Data availability. The POP model output used in this study is stored on NCAR's High Performance Storage System (HPSS); the full model output (in 5-day averages) is available with a user account by logging into cheyenne.ucar.edu and accessing the following path on HPSS: /home/bryan/johnsonb/g.e01.GIAF.T62_t12.003/ocn/hist/. Source code to run the POP2 model is available at http://www.cesm.ucar.edu/models/cesm1.0/pop2/. The CMEMS surface dynamic topography data used to produce the analysis in Figure 1 are available from http://marine.copernicus.eu/services-portfolio/access-to-products/ by searching for the Product ID SEALEVEL_GLO_PHY_L4_REP_OBSERVATIONS_008_047.

Author contributions. Primary author Andrew Delman wrote the code, carried out the analysis presented, and drafted the manuscript. Tong Lee supervised the project, providing input into the direction of the research and edits to the manuscript.

400   *Competing interests.*   There are no competing interests present in the publication of this paper.

Acknowledgements. The research was carried out at the Jet Propulsion Laboratory, California Institute of Technology, under a contract with the National Aeronautics and Space Administration (80NM0018D004) with the support of NASA Physical Oceanography. The authors would like to acknowledge Benjamin Johnson who ran the POP model configuration and made the output available, as well as Frank Bryan and Steve Yeager at the National Center for Atmospheric Research for their correspondence regarding model biases in the North Atlantic.

References

Bryan, F. O. and Smith, R. D.: Modelling the North Atlantic circulation: from eddy-permitting to eddy-resolving, International WOCE Newsletter, 33, 12–14, 1998.

Bryan, F. O., Hecht, M. W., and Smith, R. D.: Resolution convergence and sensitivity studies with North Atlantic circulation models. Part I: The western boundary current system, Ocean Modelling, 16, 141–159, 2007.

Bryan, K.: Poleward heat transport by the ocean: observations and models, Annual Review of Earth and Planetary Sciences, 10, 15–38, 1982.

Chassignet, E. P. and Marshall, D. P.: Gulf Stream separation in numerical ocean models, Geophysical Monograph Series, 177, 2008.

Chelton, D. B., Schlax, M. G., and Samelson, R. M.: Global observations of nonlinear mesoscale eddies, Prog. Oceanog., 91, 167–216, 2011.

Computational and Information Systems Laboratory: Yellowstone: IBM iDataPlex System (University Community Computing), Boulder, CO: National Center for Atmospheric Research. http://n2t.net/ark:/85065/d7wd3xhc., 2016.

Danabasoglu, G., Yeager, S. G., Bailey, D., Behrens, E., Bentsen, M., Bi, D., Biastoch, A., Böning, C., Bozec, A., Canuto, V. M., et al.: North Atlantic simulations in coordinated ocean-ice reference experiments phase II (CORE-II). Part I: mean states, Ocean Modelling, 73, 76–107, 2014.

Delman, A. S., McClean, J. L., Sprintall, J., Talley, L. D., Yulaeva, E., and Jayne, S. R.: Effects of eddy vorticity forcing on the mean state of the Kuroshio Extension, Journal of Physical Oceanography, 45, 1356–1375, 2015.

Delman, A. S., McClean, J. L., Sprintall, J., Talley, L. D., and Bryan, F. O.: Process-specific contributions to anomalous Java mixed layer cooling during positive IOD events, Journal of Geophysical Research: Oceans, 123, 4153–4176, 2018.

Dong, C., McWilliams, J. C., Liu, Y., and Chen, D.: Global heat and salt transports by eddy movement, Nature Communications, 5, 1–6, 2014.

Ducet, N., Traon, P. Y. L., and Reverdin, G.: Global high–resolution mapping of ocean circulation from TOPEX/Poseidon and ERS–1 and –2, J. Geophys. Res., 105, 19,477–19,498, 2000.

Frenger, I., Münnich, M., Gruber, N., and Knutti, R.: Southern Ocean eddy phenomenology, Journal of Geophysical Research: Oceans, 120, 7413–7449, 2015.

Gaube, P., Chelton, D. B., Samelson, R. M., Schlax, M. G., and O'Neill, L. W.: Satellite observations of mesoscale eddy-induced Ekman pumping, J. Phys. Oceanogr., 45, 104–132, https://doi.org/10.1175/JPO-D-14-0032.1., 2015.

Gent, P. R. and McWilliams, J. C.: Isopycnal mixing in ocean circulation models, Journal of Physical Oceanography, 20, 150–155, 1990.

Green, J.: Transfer properties of the large-scale eddies and the general circulation of the atmosphere, Quarterly Journal of the Royal Meteorological Society, 96, 157–185, 1970.

Griffies, S. M., Winton, M., Anderson, W. G., Benson, R., Delworth, T. L., Dufour, C. O., Dunne, J. P., Goddard, P., Morrison, A. K., Rosati, A., et al.: Impacts on ocean heat from transient mesoscale eddies in a hierarchy of climate models, Journal of Climate, 28, 952–977, 2015.

Häkkinen, S.: Variability of the simulated meridional heat transport in the North Atlantic for the period 1951–1993, Journal of Geophysical Research: Oceans, 104, 10 991–11 007, 1999.

Hall, M. M. and Bryden, H. L.: Direct estimates and mechanisms of ocean heat transport, Deep Sea Research Part A. Oceanographic Research Papers, 29, 339–359, 1982.

Hallberg, R.: Using a resolution function to regulate parameterizations of oceanic mesoscale eddy effects, Ocean Modelling, 72, 92–103, 2013.

Hausmann, U. and Czaja, A.: The observed signature of mesoscale eddies in sea surface temperature and the associated heat transport, Deep Sea Research Part I: Oceanographic Research Papers, 70, 60–72, 2012.

Hobbs, W. R. and Willis, J. K.: Midlatitude North Atlantic heat transport: A time series based on satellite and drifter data, Journal of Geophysical Research: Oceans, 117, 2012.

445 Holloway, G.: Estimation of oceanic eddy transports from satellite altimetry, Nature, 323, 243–244, 1986.

Hoskins, B. J., James, I. N., and White, G. H.: The shape, propagation and mean-flow interaction of large-scale weather systems, Journal of the Atmospheric Sciences, 40, 1595–1612, 1983.

Hsiung, J.: Estimates of global oceanic meridional heat transport, Journal of Physical Oceanography, 15, 1405–1413, 1985.

Jayne, S. R. and Marotzke, J.: The oceanic eddy heat transport, Journal of Physical Oceanography, 32, 3328–3345, 2002.

450 Johns, W. E., Baringer, M. O., Beal, L., Cunningham, S., Kanzow, T., Bryden, H. L., Hirschi, J., Marotzke, J., Meinen, C., Shaw, B., et al.: Continuous, array-based estimates of Atlantic Ocean heat transport at 26.5 N, Journal of Climate, 24, 2429–2449, 2011.

Johnson, B. K., Bryan, F. O., Grodsky, S. A., and Carton, J. A.: Climatological annual cycle of the salinity budgets of the subtropical maxima, Journal of Physical Oceanography, 46, 2981–2994, 2016.

Kirtman, B. P., Bitz, C., Bryan, F., Collins, W., Dennis, J., Hearn, N., Kinter, J. L., Loft, R., Rousset, C., Siqueira, L., et al.: Impact of ocean
455 model resolution on CCSM climate simulations, Climate dynamics, 39, 1303–1328, 2012.

Koltermann, K. P., Sokov, A. V., Tereschenkov, V. P., Dobroliubov, S. A., Lorbacher, K., and Sy, A.: Decadal changes in the thermohaline circulation of the North Atlantic, Deep Sea Research Part II: Topical Studies in Oceanography, 46, 109–138, 1999.

Large, W. G. and Yeager, S. G.: The climatology of an interannually–varying air sea flux data set, Clim. Dyn., 33, 341–364, 2009.

Lee, T. and Cornillon, P.: Propagation and growth of Gulf Stream meanders between 75 and 45 W, Journal of Physical Oceanography, 26,
460 225–241, 1996.

Maltrud, M. E. and McClean, J. L.: An eddy resolving global 1/10 ocean simulation, Ocean Modelling, 8, 31–54, 2005.

Smith, R., Jones, P., Briegleb, B., Bryan, F., Danabasoglu, G., Dennis, J., Dukowicz, J., Eden, C., Fox-Kemper, B., Gent, P., Hecht, M., Jayne, S., Jochum, M., Large, W., Lindsay, K., Maltrud, M., Norton, N., Peacock, S., Vertenstein, M., and Yeager, S.: The Parallel Ocean Program (POP) reference manual, Tech. Rep. LAUR-10-01853, Los Alamos National Laboratory, and National Center for Atmospheric
465 Research, 2010.

Smith, R. D., Maltrud, M. E., Bryan, F. O., and Hecht, M. W.: Numerical simulation of the North Atlantic Ocean at 1/10°, Journal of Physical Oceanography, 30, 1532–1561, 2000.

Stammer, D.: On eddy characteristics, eddy transports, and mean flow properties, Journal of Physical Oceanography, 28, 727–739, 1998.

Sun, B., Liu, C., and Wang, F.: Global meridional eddy heat transport inferred from Argo and altimetry observations, Nature Scientific
470 Reports, 9, 1–10, 2019.

Talley, L. D.: Shallow, intermediate, and deep overturning components of the global heat budget, Journal of Physical oceanography, 33, 530–560, 2003.

Taylor, G. I.: I. Eddy motion in the atmosphere, Philosophical Transactions of the Royal Society of London. Series A, Containing Papers of a Mathematical or Physical Character, 215, 1–26, 1915.

475 Tréguier, A.-M., Deshayes, J., Lique, C., Dussin, R., and Molines, J.-M.: Eddy contributions to the meridional transport of salt in the North Atlantic, Journal of Geophysical Research: Oceans, 117, 2012.

Tréguier, A.-M., Lique, C., Deshayes, J., and Molines, J.-M.: The North Atlantic eddy heat transport and its relation with the vertical tilting of the Gulf Stream axis, Journal of Physical Oceanography, 47, 1281–1289, 2017.

Trenberth, K. E. and Caron, J. M.: Estimates of meridional atmosphere and ocean heat transports, Journal of Climate, 14, 3433–3443, 2001.

480   Volkov, D. L., Lee, T., and Fu, L.-L.: Eddy-induced meridional heat transport in the ocean, Geophysical Research Letters, 35, 2008.

Waterman, S. and Hoskins, B. J.: Eddy shape, orientation, propagation, and mean flow feedback in western boundary current jets, Journal of
        Physical Oceanography, 43, 1666–1690, 2013.